

Hydraulic bulge testing to compare formability of continuous and stretch broken carbon fiber reinforced polymer composites

Yoni Shchemelinin, Jared W. Nelson, Cecily Ryan, Dilpreet Bajwa, Doug Cairns, Roberta Amendola

This version of the article has been accepted for publication, after peer review (when applicable) and is subject to Springer Nature's AM terms of use, but is not the Version of Record and does not reflect post-acceptance improvements, or any corrections. The Version of Record is available online at: <http://dx.doi.org/10.1007/s12289-023-01743-6>

Hydraulic bulge testing to compare formability of continuous and stretch broken carbon fiber reinforced polymer composites

Yoni Shchemelinin¹, Jared W. Nelson², Cecily Ryan¹, Dilpreet Bajwa¹, Doug Cairns¹, Roberta Amendola^{1*}

¹ Mechanical and Industrial Engineering Department, Montana State University, Bozeman, MT 59717 USA

² Sustainable Product Design & Innovation, Keene State College, Keene, NH 03435 USA

*Corresponding author

*Roberta Amendola: roberta.amendola@montana.edu; <https://orcid.org/0000-0002-0763-4984>

Dilpreet S. Bajwa: <https://orcid.org/0000-0001-9910-8035>

Douglas S. Cairns: <https://orcid.org/0000-0001-5907-7182>

Jared W. Nelson: <https://orcid.org/0000-0002-0773-6091>

Cecily A. Ryan: <https://orcid.org/0000-0001-8335-2287>

ABSTRACT

The use of carbon fiber reinforced polymer composites has increased with the increased need for high-strength, low-density materials, particularly in the aerospace industry. Stretch broken carbon fiber (SBCF) is a form of carbon fiber created by statistically distributed breakage of aligned fibers in a tow at inherent flaw points, resulting in a material constituted of collimated short fibers with an average length larger than chopped fibers. While continuous carbon fiber composites have desirable material properties, the limited ability to form in complex geometries prevents their wide adoption. SBCF composites exhibit pseudo-plastic deformation that can potentially enable the use of traditional metal forming techniques like stamping and press forming, widely used for mass production applications. To investigate the formability of carbon fiber reinforced polymer composites prepared with either continuous or stretch broken Hexcel IM-7 12K fibers and impregnated with Huntsman RDM 2019-053 resin, hydraulic bulge testing was performed at atmospheric pressure and elevated temperature to explore the strain behavior under biaxial stress conditions for the material system. Results based on deformation of surface patterning, bulge apex displacement and measurement of the bulge internal surface and volume, support the enhanced formability of the SBCF material when compared to its continuous counterpart. The SBCF enhanced formability is characterized by an axisymmetric stress response and a failure mechanism similar to the one observed for sheet metal.

Key Words: Stretch Broken Carbon Fiber, Continuous Fiber Composite, Composite Formability, Bulge Test, Multiaxial Strain, Failure

INTRODUCTION

Carbon fiber reinforced polymer composites (CFRPs) are a popular alternative to metallic materials due to their high strength, chemical resistance, and low coefficients of thermal expansion. These properties are desirable in high-performance applications such as the automotive and aerospace industries [1]. The most common forms of composites utilize two types of material, continuous or discontinuous fiber, to reinforce a resin (polymer) matrix. Typically, discontinuous composites use chopped fiber cut to small length-to-diameter ratios, randomly mixed within a resin matrix [2]. This approach leads to ease of manufacturing in processes like plastic injection molding and additive manufacturing [2]. However, the randomized arrangement of chopped fibers also reduces the benefits of the high strength of carbon fiber, often generating an orthotropic material with unpredictable properties [3,4]. Alternatively, continuous fiber composites use a base spooled tow composed of aligned continuous fibers. Each tow commonly contains 3000 (3K) to 24000 (24K) fibers, which have a nominal diameter of $\sim 5 \mu\text{m}$. A sizing solution is often added to aid with the handling and manufacturing processes [5]. Continuous fiber offers the material properties sought in the use of CFRPs, but at the cost of limited formability. In large part due to the low elongation to failure of less than 2% preventing plastic deformation [6], parts made of continuous fiber are often

restricted to either flat or low curvature shapes [3]. More complex shapes are capable of being produced using continuous fiber, but at a significant cost increase, additional processing, often requiring large autoclaves to maintain forming temperature and pressures [7], limiting wider application of the material.

Composites made of continuous fiber are strongest along the axis parallel to the fibers, while weakest in the perpendicular direction [8]. When compared to chopped fibers, the continuous fibers improve the material strength [9] by either weaving tows into fabrics [10] or aligning parallel tows into sheets (plies) later stacked with angular offsets to produce a quasi-isotropic material [11,12]. Despite the angled offset ply stacking creating a quasi-isotropic material, this manufacturing method introduces complex interactions between the micro-scale (fiber and tow) and the macro-scale (laminate) within the composite which adds complexity to forming as the stacked plies do not behave as either a conventional composite or as an isotropic material [13]. The stacking of plies results in a pliable laminate, but the inability of fibers to undergo plastic deformation limits its formability. Failure of CRFPs during forming operations is commonly due to intraply and interply shearing. Intraply shear limits the formability perpendicularly to the stack's vertical axis because fiber stiffness restricts the strain of a single ply, while interply shearing affects the relative sliding ability of the stack's sheets [14].

Stretch broken carbon fiber (SBCF) combines the formability advantages of discontinuous fibers with the mechanical strength of aligned continuous fiber [15]. The stretch-breaking process fractures individual carbon fibers at their natural flaw locations, creating a statistical distribution of lengths in the tow [6,7,16]. The resulting material is composed of aligned fibers, with an average length larger than chopped fibers, which allows for relative and independent fiber sliding resulting in the improved ability for the material to conform around tooling during forming operations [16,17]. In a first demonstration of stretch broken carbon fiber composites properties, Hexcel Corporation (Stamford, Connecticut) compared the mechanical performance of stretch broken IM7 fiber-based composites with 8552 resin matrix to those manufactured with continuous reinforcement. Properties tested at ambient conditions, cold temperature dry, and elevated temperature wet environments included 0° and 90° tension, 0° compression, open-hole tension and compression, in-plane and short beam shear, compression after impact, and pin bearing response. The results of the mechanical property testing demonstrated equivalency of a wide range of strength and stiffness related properties of the SBCF composite as compared to the continuous reinforcement [18]. These findings support the need for this current work in characterizing the formability of SBCF composites with the ultimate goal of enabling the manufacturing of complex composite geometries while maintaining the superior mechanical properties of continuous fibers composites.

To generate complex geometries, most sheet metal forming techniques involve multistep tool based, mechanical processes [19]. Intrinsic formability tests like tensile testing provide information about the basic mechanical properties of the

material, which can be related to formability independent of other characteristics like thickness and surface conditions [20]. However, the strain state is simplified and not representative of industrial forming processes. Simulative tests like the cupping (e.g Erichsen ball-punch [21,22]), reproduce the stress and strain conditions experienced during specific forming operations, and include the effects of variables such as friction with the forming tool. Alternatively, intrinsic tests such as the hydraulic bulge test [23] are employed to evaluate forming properties related to the intrinsic characteristics of the material while eliminating any effect related to the presence of a forming tool, as it uses hydrostatic pressure to apply multiaxial stress on a circular sample in a near-frictionless environment.

The response of a material to a forming process varies with the manufacturing techniques. This varied response also applies to composites which are nonhomogeneous materials characterized, in the uncured state, by viscoelastic properties that define their pseudo-ductile deformation response. During the composite forming processes, the fibers move independently in the resin matrix under the effect of the applied load. This phenomenon may result in bridging, misalignment or failure, which would later compromise the quality of the final cured product [24,25]. At present, the amount of quantifiable and comparable forming data for both continuous and discontinuous fiber reinforced polymer composites is still limited. Characterizing the deformation response of the uncured composite forming behavior is important for the manufacturing process design and for preventing the development of defects.

In this work, composite forming was evaluated by simulative forming tests. The hydraulic bulge test was adapted to composite forming conditions and used to investigate the formability of Hexcel IM-7 12K continuous and SBCF materials impregnated with Huntsman RDM 2019-053 resin, at elevated temperature (100 °C) and in an out-of-autoclave, atmospheric pressure environment.

MATERIALS AND METHODS

The composite prepreg samples for all bulge test analyses were identically prepared with either continuous or stretch broken IM-7 12K [25] tow from Hexcel (Stamford, Connecticut), impregnated with Huntsman (The Woodlands, Texas) RDM 2019-053 resin [26]. The fiber distribution of the SBCF material was assessed by random manual selection and measurement of 100 single fibers. The resulting fiber distribution frequency for the SBCF material is illustrated in Figure 1.

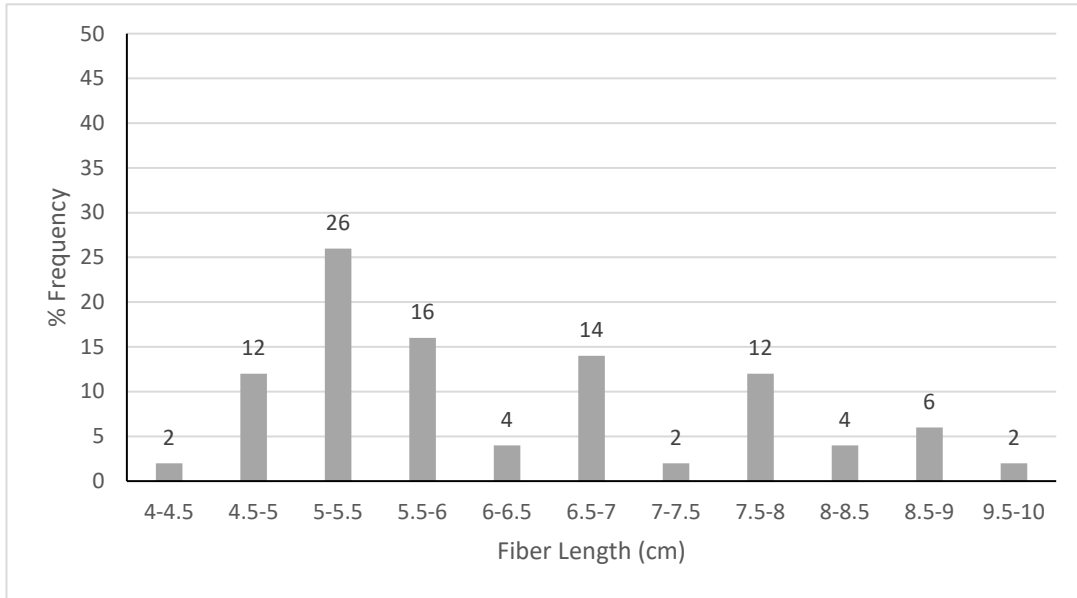


Figure 1: Fiber distribution frequency for the Hexcel stretch broken IM-7 carbon fiber material

Figure 2 shows the manufacturing process of the samples. Starting with an individual tow, the fibers were wound around a drum winder to produce a parallel fiber sheet (Figure 2 A). Two films of resin were heated to 60 °C to lower their viscosity, and then pressed against both sides of the parallel fiber sheet. Using a Professional Laminating Systems (Hamilton, Montana) P1227hp, the stack of resin and fiber tows was press-rolled with the first set of rollers heated to 121 °C (Figure 2 B), and passed through the rollers twice, at a rate of 76 mm/min under the “maximum pressure” setting available for the machine and being reversed after the first run. This process produced a prepreg sheet of parallel fibers (Figure 2 C), which was then cut into 9 in. (228.6 cm) diameter circles (Figure 2 D), before stacking into an eight ply quasi-isotropic [0/45/90/-45]_s sample. The laminate was then heated to 30 °C and pressed under vacuum bag to a reduction of 80 KPa, for 15 minutes to compact the sample and allow for a more homogeneous distribution of the uncured resin within the eight layers. The average thickness of the prepared samples was 1.8±0.2 mm.

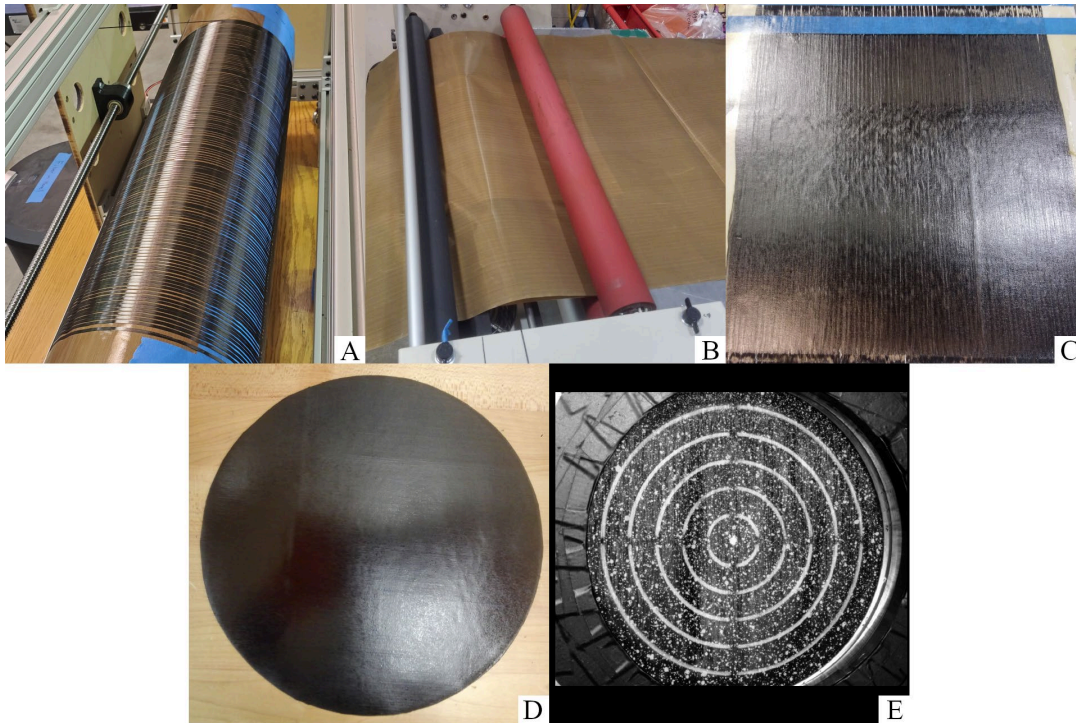


Figure 2: Bulge test sample preparation process: (A) Fiber tow winding to make a sheet, (B) press-rolling between two layers of resin, (C) prepreg sheet, (D) cut circular sample and, (E) applied Digital Image Correlation (DIC) and forming ring patterns

To track sample deformation, two patterns were sprayed on the outer surface (Figure 2 E); a speckle pattern for visibility to the Digital Image Correlation (DIC) camera system and a custom ring pattern for strain analyses. The speckle pattern used on the samples was inverted compared to a traditional DIC pattern [27], using a black base coat with white speckles on top. This change was made as it was found, during testing with DIC, to improve tracking as the base coat matched the black color of the underlying prepreg. A GOM (Braunschweig, Germany) ARAMIS 3D DIC system using 50-mm lenses was used to track the strain of the top surface in three dimensions.

The additional, custom five-ring pattern based on ASTM E2218-15 [28], was added to aid with strain analysis. The five rings, measured outer to inner, had diameters of 63.5, 50.8, 38.1, 25.4, and 12.7 mm, respectively, with a 1.3-mm diameter center dot used as reference for alignment of the system. By measuring the deformation of the rings, the major and minor strains were evaluated independently of the DIC tracking.

A schematic of the bulge test is shown in Figure 3. This diagram shows a simplified cross-sectional view of the bulge testing assembly with the major components labeled. The sample secured by the friction rings is placed within the unit before the application of the hydraulic pressure (water).

For good consistency between tests, measurable sample clamping was adopted: a 108.5 N-m torque force is used on each of the clamping bolts, validated using a torque-limiting bit attached to a hammer drill driver. Preliminary testing validated that the torque applied to the bolts produces a symmetrical loading on the test samples. Two 1.3-mm thick aluminum friction rings were also used to mitigate slipping of the sample during testing. An outer ring was placed underneath the sample and an inner ring was placed above it. The final configuration of the clamped sample is shown in Figure 4.

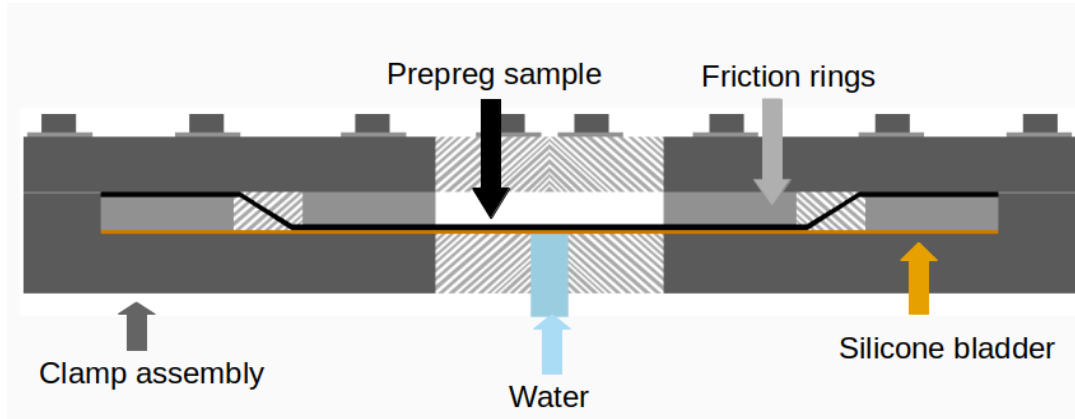


Figure 3: Diagram of the bulge testing assembly

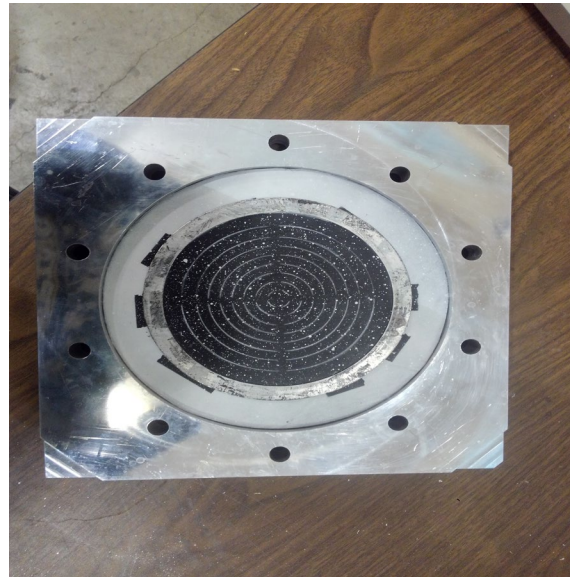


Figure 4: Final configuration of the clamped sample with aluminum friction rings

Figure 5 shows the bulge test setup. The system was pressurized by water (Figures 3 and 5). A 1.3-mm thick silicone bladder with a diameter of 228.6 mm was used to prevent the water from interfering with the prepreg sample. A 3447-KPa rated one-way valve in the bulge tester pump prevented water from escaping the bladder during testing.

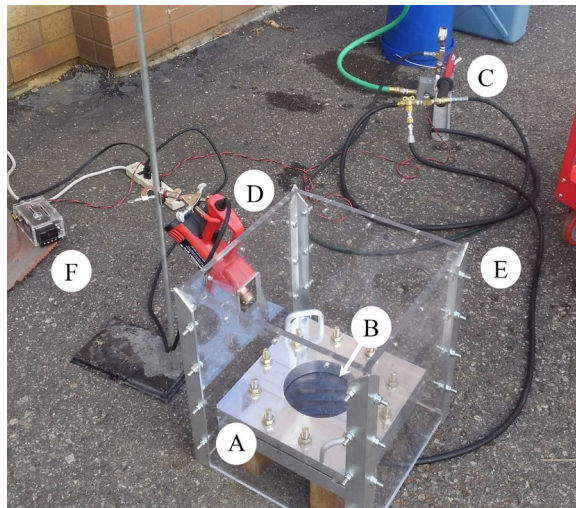


Figure 5: Bulge tester assembly: (A) bulge tester clamping assembly, (B) clamped sample, (C) water pump, (D) heat gun, (E) safety enclosure, (F) and pressure transducer.

To track the sample center vertical displacement, a Wenglor (Beavercreek, Ohio) OPT2011 laser rangefinder was added to the GOM 3D DIC camera assembly. For each recorded DIC image, the peak pump pressure was tracked. All tests were conducted at an elevated temperature of 100 °C to ensure low resin viscosity. A Master Appliance (Racine, Wisconsin) PH-1600 self-regulating heat gun was used to maintain the set temperature.

The DIC camera system was used to track the speckle pattern (Figure 2 E) and the deformation of the top surface in the 3D space (Figure 6), providing both strain and displacement data during testing. Equations 1 and 2 were adapted from the ASTM E2218-15 standard and were used to translate the change in ring width (perpendicular to tow axis) and height (parallel to tow height) into minor and major strains, respectively. For both SBCF and continuous samples, the forming pattern ring analysis numbering is the same: ring 1 refers to the innermost ring, and the number increases with radius to the outermost ring 5. Additional analysis found it to be useful to include the behavior of the outer diameter of the sample, where the clamping of the bulge tester starts, and is labeled as the sample OD.

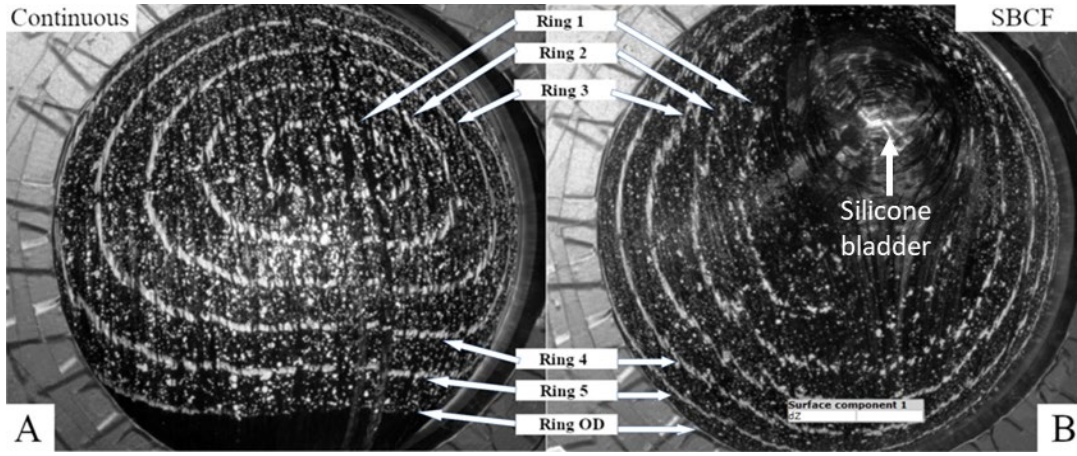


Figure 6: (A) DIC image of bulge testing at sample failure, with continuous fiber, (B) and SBCF. The labels point toward the forming pattern ring numbers used with equations 1 and 2.

$$Major(Vertical)Strain = \frac{finalring_{height} - initialring_{height}}{initialring_{height}} * 100 \quad (1)$$

$$Minor(Horizontal)Strain = \frac{finalring_{width} - initialring_{width}}{initialring_{width}} * 100 \quad (2)$$

Testing of all samples was conducted until failure. To extract nominal deformation behavior, the recorded measurements and calculated strain values were averaged. Each sample required a different amount of time to reach failure which resulted in a different number of DIC image data for each test. For this reason, data were aligned on a normalized scale. This alignment was accomplished by placing the normalized values on the same time axis, at 10-second intervals, selecting the closest appropriate time slot. Linear interpolation was used to fill the strain values between missing time slots.

The Knud-Thomsen formula [29], which relies on the assumption that the sample deformation is an oblate spheroid, was utilized for comparing the surface area of the bulged samples. These calculations considered the diameter of the bulge tester for the evaluation of the initial area and combined it with the laser rangefinder readings for the deformed area.

After testing, bulged samples were left to cure at room temperature to evaluate internal surface, volume, and cross-sectional thickness distribution. This curing process was slow and did not alter the geometry of the samples after testing. To confirm that the size of the samples was maintained, the cured samples were measured with calipers. The cured heights of the bulges were found to reflect the original laser rangefinder values.

Mapping of the internal surface contours were created using an Artec3D (Santa Clara, California) Spider structured light 3D scanner. The scanning process produced a 3D surface mesh file of the innermost layer of the bulges. This process included excess fringing created by the scans, which was then trimmed to leave the bulges as the only mesh remaining. Once imported into 3DS Max, a mesh was scaled so that the forming diameter matched the measured value to produce an accurate measurement of the surface area. Examples of the internal surface scans of continuous and SBCF samples are shown in Figure 7.

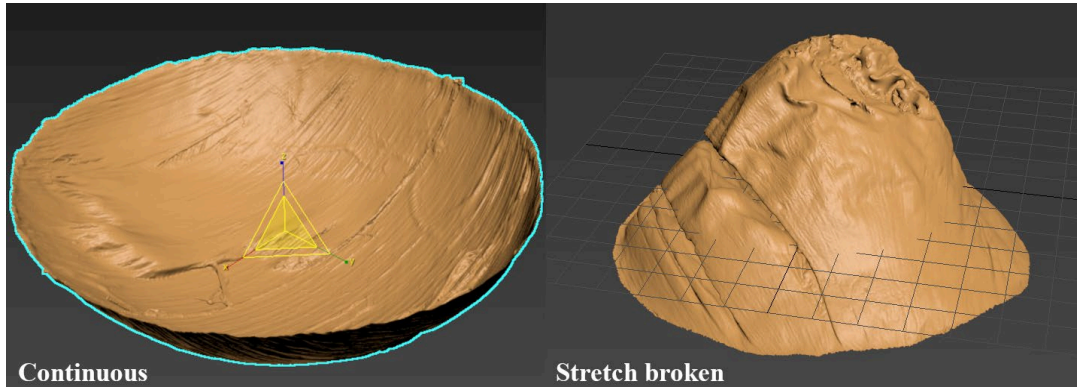


Figure 7: Artec3D Spider structured light 3D surface scan examples of a continuous and SBCF sample

For further comparison of the forming behavior, in addition to the measurement of the surface area, the internal volume of the bulged samples was also evaluated using the water displacement method. The measured values were then compared with the oblate spheroid theoretical volume. Cured samples were cut in half to evaluate the material cross sectional thickness distribution. An AmScope (Irvine, California) MU1000 optical stereo microscope was used to record images of the cross-sections at specific locations namely at the base of the bulge, at the bulge apex, and at the slipped areas when present.

RESULTS AND DISCUSSION

The vertical deformation recorded at failure by the laser rangefinder, corresponding to ~ 60 mm, was found to be similar for SBCF and continuous fiber. Figures 8 and 9 show the bulge vertical displacement, measured by the laser rangefinder as function of time and of water pressure respectively. The inherent laser rangefinder linear deviation was ± 15 mm, as defined by its user manual. When measured with calipers, the halved samples average bulge height was recorded to be 54.4 ± 0.4 mm confirming that measurements were within the rangefinder statistical error.

Figure 8 shows the averaged laser rangefinder deflection measurement versus time. Sample failure is represented by vertical displacement steady state values vs. increasing time. All SBCF samples reached failure after an average of ~ 800 s earlier than continuous fiber samples which failed after ~ 1470 s.

Figure 9 shows the laser rangefinder vertical displacement vs. forming pressure. For both continuous and SBCF samples, pressure started to decrease after reaching the peak value and until failure while vertical deflection and straining continued to increase. The average peak pressure recorded for the continuous samples was 710 KPa corresponding to 33.2 mm of vertical displacement. The SBCF samples reached an average peak pressure of to 350 KPa and 44.1 mm of vertical displacement. After reaching the peak pressure, the final average vertical displacement for continuous samples was 55.9 mm, and 59.7 mm for SBCF samples.

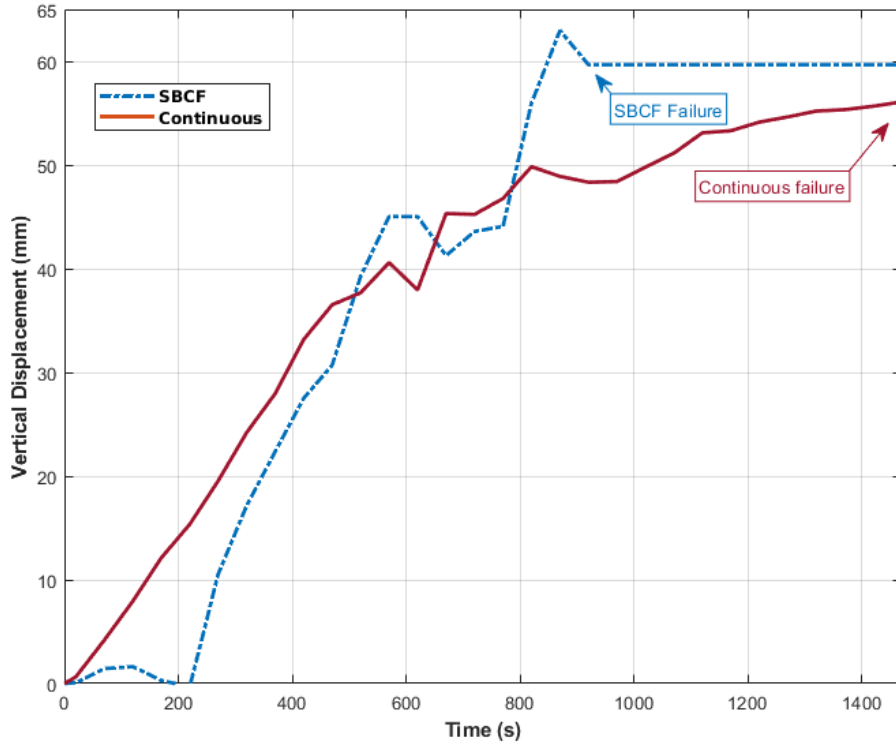


Figure 8: Average laser rangefinder deflection measurement vs. time for continuous and SBCF samples

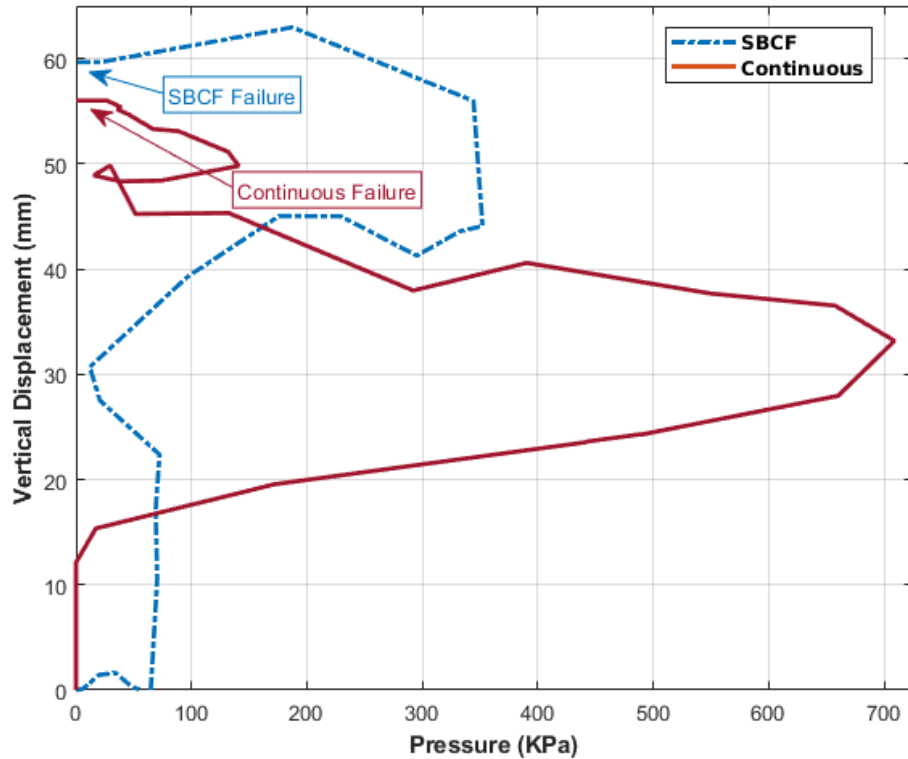


Figure 9: Average laser rangefinder deflection measurement vs. pressure for continuous and SBCF samples

For a sheet metal to form properly during bulge testing, high deflection at the dome apex reached in a short time and with small loading is desired. The SBCF samples demonstrated better formability when compared to continuous samples as they reached a higher vertical displacement, also visible in Figure 7, in a shorter time at lower peak pressure.

Equations 1 and 2, were used to calculate the strain experienced by the samples by evaluating the deformation for each ring shown in Figure 6. Figure 10 shows the horizontal and vertical strain values averaged across all the forming rings to produce single horizontal and vertical strain values with pressure for each material type. This analysis was used to see if the 8-ply quasi-isotropic layer stacking creates an angle-independent, axisymmetrical response to the forming pressure loading. Figure 10 shows the strain comparison across the sample from the center to periphery, calculated as single per-ring strain by averaging the horizontal and vertical strains as function of the forming pressure.

All continuous fiber samples experienced slippage as shown by the displacement of the OD ring (Figure 6 A), i.e. material from the clamped portion of the bulge tester was pulled into the viewing window, compressing the forming pattern in the

vertical axis. This compression translated into the seemingly negative strain in both the average vertical and per-ring strains in the analysis shown in Figures 10 and 11. This behavior was not observed for the SBCF samples, as demonstrated by the similar vertical and horizontal strains with no negative values.

The per ring strain analysis shown in Figure 11 combined the vertical and horizontal strains for each ring to show the radial strain behavior. Due to the non-axisymmetric behavior of the continuous samples, the per-ring strain overestimates the strain in the vertical direction, while underestimating the horizontal one. On the contrary, SBCF fibers had a strong axisymmetric response, where the per-ring strain was highly representative of the sample strain as a function of distance from the center of the sample.

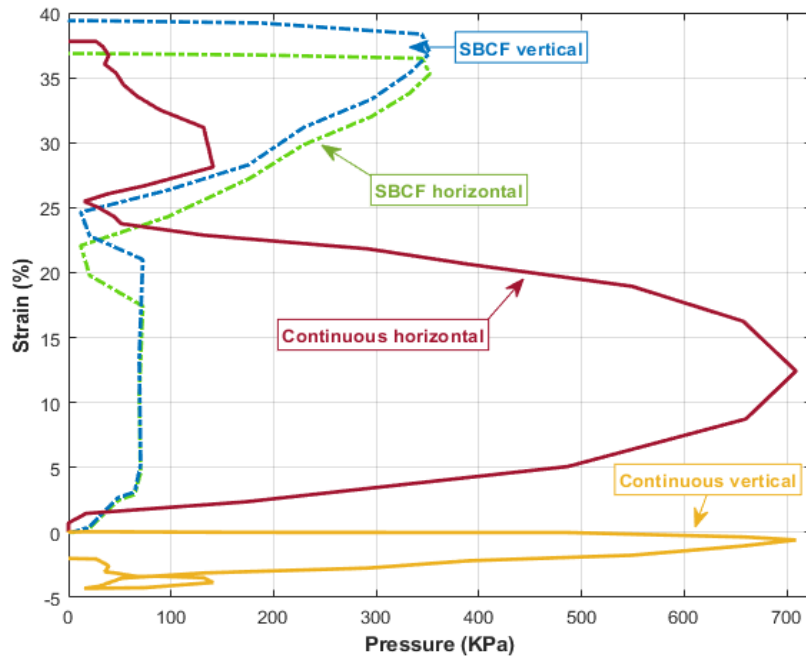


Figure 10: Comparison of the average horizontal and vertical strains vs. pressure for continuous and SBCF samples

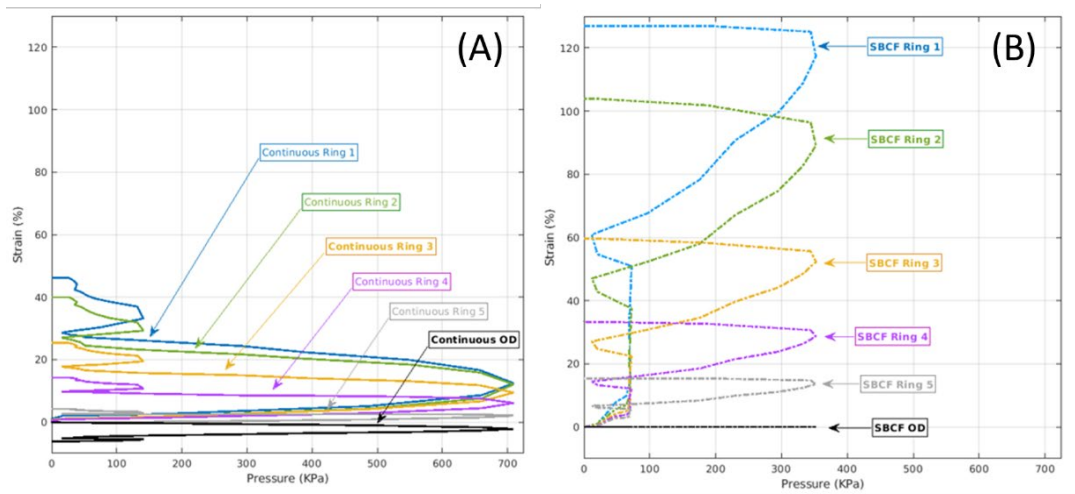


Figure 11: Per-ring horizontal and vertical strains comparison vs. pressure for (A) continuous and (B) SBCF samples

To evaluate the final strain at failure, the average of the horizontal and vertical strains for each forming ring across the two types of samples is compared in Figure 12. These strain values correspond to the final data point for each ring number shown in figure 11. The same deformation trend was observed for both the continuous and the SBCF material with the average failure horizontal and vertical % strains decreasing from the inner ring to the outer ring however, larger values of the deformation are achieved by the SBCF material when compared to the continuous one.

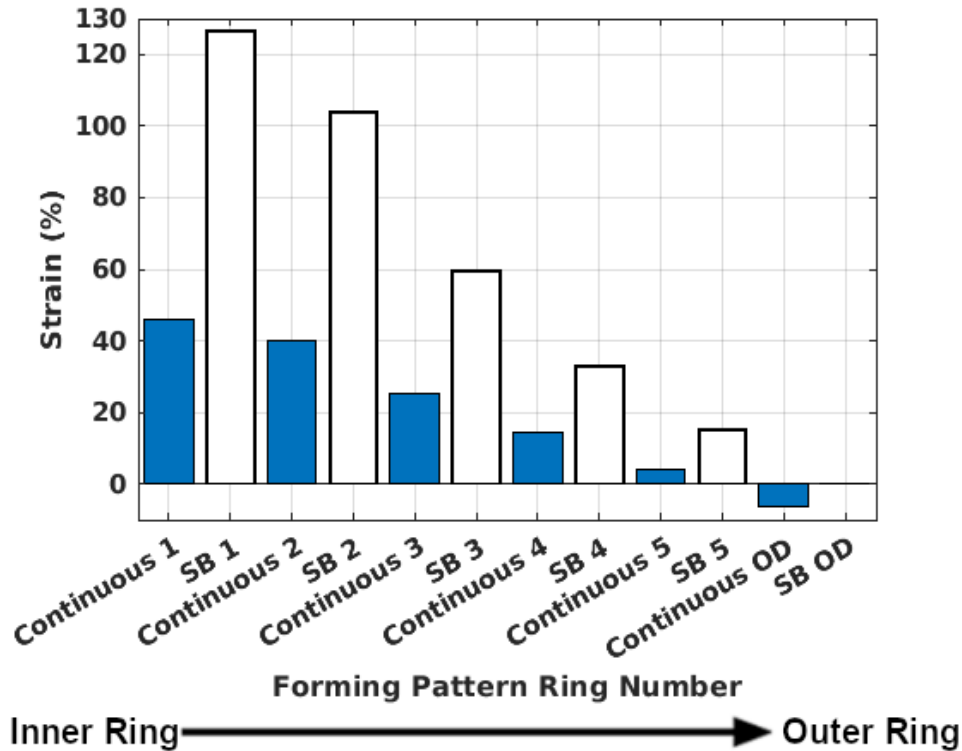


Figure 12: Average failure horizontal and vertical % strains for each forming pattern ring, for both continuous and SBCF samples

The data represented in Figures 10 and 12 well support the improved formability of SBCF samples when compared to the continuous ones. Figure 10 shows that the maximum horizontal strain for continuous samples at the peak pressure of ~717 KPa psi was <20%, with small negative vertical strain. A >50% lower peak pressure of ~345 KPa produced similar horizontal strain for SBCF and a vertical strain of >35%. Figure 12 further shows the innermost ring (ring 1) reaching an average strain of ~45% for continuous samples and of 130% for the SBCF ones. The outer diameter (OD) experienced a negative strain of ~-8% for the continuous samples due to material slipping behavior decreasing the ring diameter in the vertical axis, while it demonstrated no strain for SBCF samples. The SBCF no-slip behavior is particularly relevant during forming processes of complex parts as it holds the potential to reduce flange wrinkling issues and to enable wide application of out-of-autoclave prepreg processing (e.g. vacuum bag method) because of the reduced pressure required to achieve larger material deformation when compared to continuous fiber samples.

The visual inspection of the cured samples that were cut in half, revealed an increased cross-sectional thickness at the slipped side of the continuous samples when compared to the un-slipped side. An even cross-sectional thickness distribution was instead observed for the SBCF samples. Figure 13 shows a simplified diagram of the uneven cross-sectional thickness distribution of the

continuous samples. Points a, b and c identify the selected sampling locations for microscopy analyses along with images of cross-sections sampling later detailed in Figures 14 to 16. The cross-section of continuous samples depicted in Figure 14, was found to be uniform and of comparable thickness at the no-slip side and at the bulge apex locations, as shown in Figures 14 A and 14 B respectively. Instead, at the slipped side location a larger thickness and the presence of defects were observed as shown in Figure 14 C.

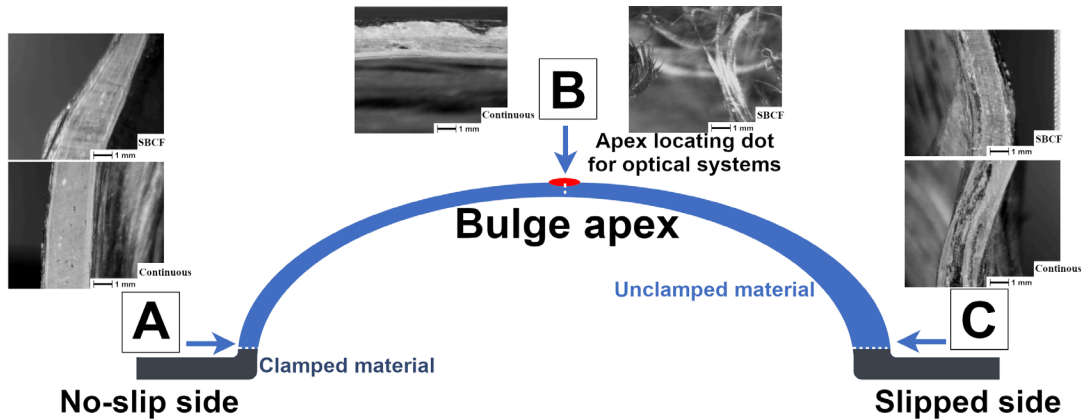


Figure 13: Schematic of the location of cross section sampling for bulged samples after curing at room temperature in ambient air with corresponding optical microscope images of continuous and SBCF.

Measurements were then performed to quantify the change in the cross-sectional thickness. An average thickness of 1.83 ± 0.08 mm was measured at the base and at the apex of the bulge when slippage did not occur, which corresponds to a 1.6% cross sectional reduction. Instead, when slippage occurred, the thickness at the base of the bulge increased to 2.49 ± 0.5 mm while the thickness at the apex remained unchanged. Additional microscopy analyses were performed to understand the nature of the defects identified at the slipped side of the sample. Figure 15 shows a detailed comparison between the no-slip (Figure 15 A) and the slipped side (Figure 15 B) cross sections of the continuous fiber composite samples. The no-slip side presents uniform material distribution (Figure 15 A) while, when slippage is observed, the material is compromised by delamination and large voids within the cross section (Figure 15 B). The presence of such voids explains the increased cross-sectional thickness as material is being displaced at the base of the bulge due to the limited ability to stretch of the continuous fibers.

When compared to continuous samples, the application of biaxial strains during forming tests of SBCF samples caused localized through-thickness thinning (necking) and subsequent failure [28]. Figure 16 shows the optical microscope images of the SBCF sample's cross-sections after curing at room temperature in ambient air. Matching the naming convention of Figure 13, the no-slip side cross section characterized by uniform material distribution and absence of voids is shown in Figure 16 A. The through-thickness failure is depicted in Figure 16 B and

the slipped side cross section, with a material thickness comparable to Figure 16 A is shown in Figure 16 C. This phenomenon, which mimics the behavior of metallic sheets, revealed SBCF samples superior formability. when compared to the continuous fiber composite samples, which instead demonstrated limited formability by maintaining significant thickness at the apex during failure (Figure 14 B).

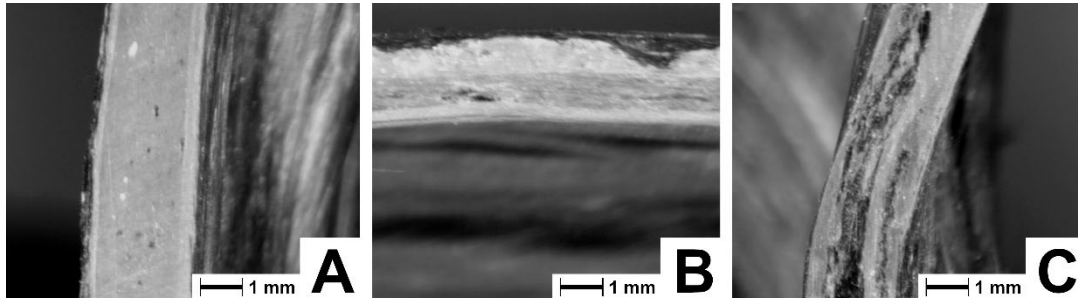


Figure 14: Optical microscope images of cross section sampling for bulged continuous fiber composite samples after curing at room temperature in ambient air. (A) No-slip side, (B) bulge apex and (C) slipped side

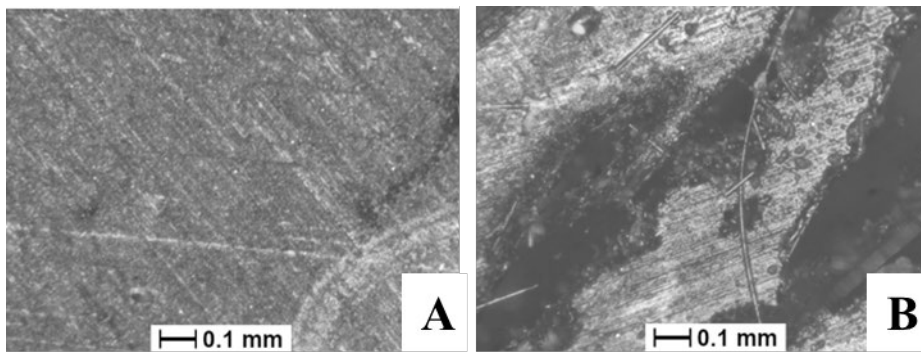


Figure 15: comparison between the cross sections of the no-slip (A) and the slipped side (B) of the continuous fiber composite samples after curing at room temperature in ambient air

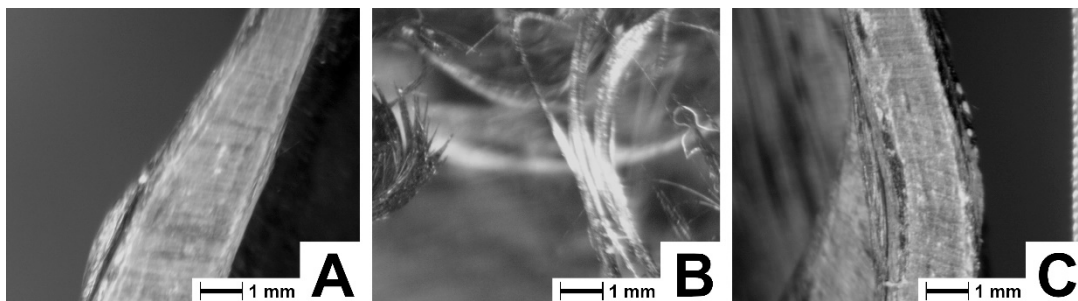


Figure 16: Optical microscope images of cross section sampling for bulged SBCF composite samples after curing at room temperature in ambient air. (A) No-slip side, (B) bulge apex and, (C) slipped side

To further characterize the continuous and SBCF materials forming behavior, the internal volume and surface area measurements of bulged and cured samples were compared with the theoretical values calculated using the oblate spheroid assumption. Table 2 summarizes the average values of the internal theoretical surface area (SA_t), theoretical volume (V_t), measured surface area (SA_m), measured volume (V_m), the % difference between the theoretical and measured surface area (ΔSA) and % difference between the theoretical and measured volume (ΔV). A negative change in ΔSA was observed for both materials as the measured quantities were larger than the theoretical values. The measured internal volumes were instead found to be smaller than the theoretical ones for both material types.

Table 2 shows considerable ΔSA and ΔV values therefore, the oblate spheroid may not be the proper method to evaluate and predict the bulging behavior of the composite materials; however, the larger values recorded for the SBCF samples supports the enhanced formability of the SBCF material when compared to the continuous samples.

Table 2: Average of the theoretical and measured surface areas and internal volumes of cured bulged continuous and SBCF samples

	Continuous	SBCF
SA_t (mm ²)	30260±1000	31810±2100
SA_m (mm ²)	32390±3900	34710±1600
ΔSA (%)	-7	-9.1
V_t (ml)	709.8±41	754.1±77
V_m (ml)	576.7±44	600.3±101
ΔV (%)	18.8	20.4

Wrinkling and warping on the inner surface of the SBCF sample were observed after testing. As the bulge testing was performed in the direction opposite of gravity, it is likely that such defects appeared after failure in absence of the applied hydraulic pressure. While this phenomenon is not to be considered an ideal behavior, it does at the same time, demonstrate the SBCF samples enhanced formability as the still uncured material can further naturally form under the effect of gravity rather than remaining deformed in the smooth outline of the pressurized shape like the continuous samples.

CONCLUSIONS

The forming behavior of carbon fiber reinforced polymer composites prepared with either continuous or stretch broken Hexcel IM-7 12K fiber impregnated with Huntsman RDM 2019-053 resin was investigated with the use of hydraulic bulge testing. Results showed that both materials demonstrated similar vertical displacement at failure, but the SBCF required lower peak pressure when compared to continuous fiber samples. The strain of SBCF samples, assessed using a customized ring surface pattern, showed angular symmetry, with a maximum strain

at the center which trended to zero at the outer diameter, while continuous fiber samples showed strong axis-asymmetry caused by material slippage at the outer diameter. SBCF samples offer enhanced forming behavior when compared to continuous fiber samples by achieving greater strain values at smaller forming pressures, while demonstrating sample axisymmetry and no sample slippage. It was also observed that SBCF samples mimic the forming behavior of metallic sheets as the application of biaxial strains caused localized cross-sectional thickness thinning (necking) and subsequent failure. This investigation implies that the SBCF material could enable wider application of out-of-autoclave prepreg processing (e.g vacuum bag method) as well as traditional metal forming processes (e.g. drawing) because of the reduced pressure required to achieve larger material deformation when compared to continuous fiber material.

DECLARATIONS

Funding and/or Competing interests

This work was supported by the US Department of the Army under the award number W911W6-18-C-0050. The views and conclusions contained in this document are those of the authors and should not be interpreted as necessarily representing the official policies, either expressed or implied, of the Government.

The authors have no competing interests to declare that are relevant to the content of this article.

REFERENCES

1. Hull D, Clyne, T. W. (1981) B. *An Introduction to Composite Materials*, Cambridge Solid State Science Series, 9-38
2. Ning, F., Cong, W., Hu, Z., and Huang, K. (2017). *Additive manufacturing of thermoplastic matrix composites using fused deposition modeling: A comparison of two reinforcements*. Journal of Composite Materials, 51(27), 3733-3742.
3. Lee, K., Lee, S. W., & Ng, S. J. (2008). *Micromechanical modeling of stretch broken carbon fiber materials*. Journal of composite materials, 42(11), 1063-1073.
4. Li, Y., Chen, Z., Xu, H., Dahl, J., Zeng, D., Mirdamadi, M., and Su, X. (2017). *Modeling and simulation of compression molding process for sheet molding compound (SMC) of chopped carbon fiber composites*. SAE International Journal of Materials and Manufacturing, 10(2), 130-137.
5. Eyckens, D. J., Arnold, C. L., Simon, Ž., Gengenbach, T. R., Pinson, J., Wickramasingha, Y. A., & Henderson, L. C. (2021). *Covalent sizing surface modification as a route to improved interfacial adhesion in carbon fibre-epoxy composites*. Composites Part A: Applied Science and Manufacturing, 140, 106147.

6. Den Uijl, N. J., & Carless, L. J. (2012). *Advanced metal-forming technologies for automotive applications*. In *Advanced materials in automotive engineering* (pp. 28-56). Woodhead Publishing.
7. Schuster, J., Kazmi, S. M. R., & Lutz, J. (2015, July). *Manufacturing and Testing of Curved Fibrecomposites Using Vacuum Assisted Resin Transfer Moulding (VARTM)*. In *20th International Conference on Composite Materials (ICCM-20)*, Copenhagen (pp. 19-24).
8. F.C. Campbell, *Structural Composite Materials*, ASM International, Ohio, 2010.
9. Medina, C., Canales, C., Arango, C., & Flores, P. (2014). *The influence of carbon fabric weave on the in-plane shear mechanical performance of epoxy fiber-reinforced laminates*. *Journal of Composite Materials*, 48(23), 2871-2878.
10. Wang, F. (2017). *Carbon fibers and their thermal transporting properties*. In *Thermal transport in carbon-based nanomaterials* (pp. 135-184). Elsevier.
11. Rahmani, H., Najafi, S. H. M., Saffarzadeh-Matin, S., & Ashori, A. (2014). *Mechanical properties of carbon fiber/epoxy composites: Effects of number of plies, fiber contents, and angle-ply layers*. *Polymer Engineering & Science*, 54(11), 2676-2682.
12. Rahmani, H., Najafi, S. H. M., & Ashori, A. (2014). *Mechanical performance of epoxy/carbon fiber laminated composites*. *Journal of Reinforced Plastics and Composites*, 33(8), 733-740.
13. Janicki, J. C., Egloff, M. C., Amendola, R., Ryan, C. A., Bajwa, D. S., Dynkin, A., & Cairns, D. S. (2021). *Formability Characterization of Fiber Reinforced Polymer Composites Using a Novel Test Method*. *Journal of Testing and Evaluation*, 50(2).
14. G. Jacobsen, W. Schimpf, *Process Development and Characterization of Stretch Broken Carbon Fiber Materials*, Hexcel Corp., Utah, 2008.
15. Şükür, E. F., Türköz, M., Dilmeç, M., Halkacı, H. S., and Halkacı, M. (2016). *Comparison of flow curves of AA 5457-O sheet material determined by hydraulic bulge and tensile tests at warm forming temperatures*. *Journal of Testing and Evaluation*, 44(2), 952-966.
16. Srbislav, A., Milentije, S., Dragan, A., & Vukić, L. (2009). *Variation of Normal Anisotropy Ratio "r" during Plastic Forming*. *Journal of Mechanical Engineering*, 55(6), 392-399.
17. D. Eyckens, C. Arnold, Ž. Simon, T. Gengenbach, J. Pinson, Y. Wickramasingha, L. Henderson. (2021). *Covalent sizing surface modification as a route to improved interfacial adhesion in carbon fibre-epoxy composites*, *Composites Part A: Applied Science and Manufacturing*, Volume 140.
18. Jacobsen, G. (2010). *Mechanical characterization of stretch broken carbon fiber materials IM7 fiber in 8552 resin*, SAMPE 10 Spring Symposium Technical Conference Proceedings (pp. 17-20).
19. Pavan kumar, J., Uday kumar, R., Ramakrishna, B., Ramu, B., & Baba Saheb, K. (2018, December). *Formability of sheet metals—A review*. In *IOP*

- Conference Series: Materials Science and Engineering (Vol. 455, No. 1, p. 012081). IOP Publishing.
20. Bruschi, S., Altan, T., Banabic, D., Bariani, P. F., Brosius, A., Cao, J., Tekkaya, A. E. (2014). *Testing and modelling of material behaviour and formability in sheet metal forming*. CIRP Annals, 63(2), 727-749.
 21. ASTM International. E643-15 Standard Test Method for Ball Punch Deformation of Metallic Sheet Material. West Conshohocken, PA; ASTM International, 2015.
 22. ASTM International. E2712-15 Standard Test Methods for Bulge-Forming Superplastic Metallic Sheet. West Conshohocken, PA; ASTM International, 2015.
 23. Miranda, S. S., Santos, A. D., Amaral, R. L., Malheiro, L. T. (2019). *Characterization and Formability Analysis of a Composite Sandwich Metal-Polymer Material*. In Materials Design and Applications II (pp. 487-508). Springer, Cham.
 24. Hueber, C., Fischer, G., Schwingshandl, N., & Schledjewski, R. (2019). *Production planning optimisation for composite aerospace manufacturing*. International Journal of Production Research, 57(18), 5857-5873.
 25. *Hextow IM7 carbon fiber datasheet*, Hexcel Corp., Connecticut, 2020
 26. *Huntsman RDM2019-053 datasheet*, Huntsman, Texas, 2020.
 27. Sur, F., Blaysat, B., & Grédiac, M. (2018). *Rendering deformed speckle images with a Boolean model*. Journal of Mathematical Imaging and Vision, 60(5), 634-650.
 28. ASTM International. E2218-15 Standard Test Method for Determining Forming Limit Curves. West Conshohocken, PA; ASTM International, 2015
 29. Weisstein, Eric W. "Oblate Spheroid." From *MathWorld*--A Wolfram Web Resource. <https://mathworld.wolfram.com/OblateSpheroid.html>